

## FIRST RESULTS FROM THE HUBBLE OPAL PROGRAM: JUPITER IN 2015

AMY A. SIMON<sup>1</sup>, MICHAEL H. WONG<sup>2</sup>, AND GLENN S. ORTON<sup>3</sup>

<sup>1</sup> NASA Goddard Space Flight Center Solar System Exploration Division (690) Greenbelt, MD 20771, USA; amy.simon@nasa.gov

<sup>2</sup> University of California at Berkeley Astronomy Department Berkeley, CA 94720-3411, USA

<sup>3</sup> Jet Propulsion Laboratory/California Institute of Technology M/S 183-501, 4800 Oak Grove Drive Pasadena, CA 91109, USA

Received 2015 July 23; accepted 2015 September 3; published 2015 October 7

### ABSTRACT

The Hubble 2020: Outer Planet Atmospheres Legacy program is generating new yearly global maps for each of the outer planets. This report focuses on Jupiter results from the first year of the campaign. The zonal wind profile was measured and is in the same family as the *Voyager* and *Cassini* era profiles, showing some variation in mid- to high-latitude wind jet magnitudes, particularly at  $+40^\circ$  and  $-35^\circ$  planetographic latitude. The Great Red Spot continues to maintain an intense orange coloration, but also shows new internal structures, including a reduced core and new filamentary features. Finally, a wave that was not previously seen in Hubble images was also observed and is interpreted as a baroclinic instability with associated cyclone formation near  $16^\circ$  N latitude. A similar feature was observed faintly in *Voyager 2* images, and is consistent with the Hubble feature in location and scale.

*Key words:* planets and satellites: atmospheres – planets and satellites: gaseous planets – planets and satellites: individual (Jupiter) – waves

### 1. INTRODUCTION

For the outer planets, Jupiter, Saturn, Uranus and Neptune, many atmospheric phenomena occur on timescales of years to decades, while transient events often occur with little notice. Long time-base observations of the outer planets are critical in understanding the atmospheric dynamics and evolution of gas giant planets. The Hubble 2020: Outer Planet Atmospheres Legacy (OPAL) program provides for yearly outer planet monitoring using the Wide Field Camera 3 (WFC3) for the remainder of Hubble’s lifetime as a lasting legacy of increasingly valuable data for time-domain studies. The program began with Hubble observing Cycle 22 with Uranus in 2014 (Wong et al. 2015) and Jupiter in early 2015.

The main goal of OPAL is to observe each of the giant planets for long-duration time-domain studies of storm activity, wind field variability, and changes in aerosol distributions and colors. These data can also be used with older Hubble and other spacecraft data sets to expand the time domain even further. As an example, Jupiter was studied extensively with Hubble Wide Field Planetary Camera 2 over 15 years, and has been periodically visited by a number of other spacecraft, include the two *Voyagers*, *Cassini*, and *New Horizons*. Each of these provided a single snapshot in time, but when placed in context contribute to a larger picture of the evolving atmosphere. The *Galileo* spacecraft observed the planet for eight years, but could not provide global coverage, due to the limited bandwidth available with the low-gain antenna and the lack of a wide-angle camera.

A crowning feature of the OPAL program is that, for each planet, two full rotations are acquired in a variety of filters optimized to allow the best science return for that target. This means that, in addition to global views or zonal wind profiles, we will also be able to obtain global two-dimensional wind fields each year for each planet. This unprecedented data set is beginning to allow new insights into the complex atmospheric circulations and their variations. In addition, this coverage will allow a complete census of visible storms and any serendipitous features present in each year. The OPAL data are intended to be of broad general interest, and are immediately available in

the MAST archive with no proprietary period. In this paper, we outline preliminary results and discoveries made in the first observation set of Jupiter.

### 2. DATA

#### 2.1. Observations

Table 1 summarizes the WFC3 data acquired for Jupiter on 2015 January 19. All images were acquired with the UVIS detector, whose pixel scale is about 0.04 arcsec (Dressel 2015). Filters were chosen to allow maximum cloud contrast for wind tracking (typically the red continuum wavelengths), altitude discrimination (UV and methane-gas absorption wavelengths) and color analyses (blue and green wavelengths). To generate a global map of Jupiter requires 6–7 consecutive orbits of Hubble (each 96-minute orbit allows about 52 minutes of target visibility between Earth occultations). Due to the Earth’s South Atlantic Anomaly, which introduces a higher rate of high-energy particle hits on the detectors, it is sometimes necessary to skip an orbit with a more direct passage into this region of Earth’s magnetic field. *Hubble Space Telescope* gyroscope bias reset activities also prevent blocks of more than seven consecutive orbits from being scheduled. Thus, the Jupiter data skip an orbit in-between maps. Because of overlap at the end of a seven-orbit sequence some regions were visible with an  $\sim 10$ -hr separation, while a limited longitude range also had a 20-hr separation. Finally, the observations were also designed to allow for small time separations within an orbit, repeating the red filter at the beginning and end of each sequence.

#### 2.2. Data Processing

All images were retrieved after the standard Hubble pipeline processing was performed. Fringing introduces photometric error due to multiple internal reflections within the detector, since silicon is increasingly transparent at long wavelengths. The photometric error is spatially variable across the image and highly dependent on the wavelength of illumination. The effect is significant only for narrowband filters at wavelengths

**Table 1**  
OPAL Data Acquired

Rotation 1 (2015 January 19 02:00 to 12:30 UT)			
Filter	Minnaert $k$	Notes	Analyses
F631N	.999	...	Spectral, Winds
F502N	.950	...	Spectral, Waves
F395N	.850	...	Spectral, Waves
F467M	n/a	Saturated	Spectral
FQ889N	1.00	Slight saturation in GRS core in 10:28 UT frame, corrected for fringing	Spectral, Waves
F658N	.999	...	Spectral
F275W	n/a	...	Spectral, Waves
F547M	.970	Slight saturation near the equator	Spectral
Rotation 2 (2015 January 19 15:00 to 23:40 UT)			
Filter	Minnaert $k$	Notes	Analyses
F631N	.999	...	Spectral, Winds
F502N	.950	...	Spectral, Waves
F395N	.850	...	Spectral, Waves
F467M	n/a	Saturated	Spectral
FQ889N	1.00	Corrected for fringing	Spectral, Waves
F658N	.999	...	Spectral
F275W	n/a	...	Spectral, Waves
F343N	.850	...	Spectral

>650 nm (Wong 2010). Standard flatfield corrections remove fringing error when the target's spectral energy distribution is the same as the continuum spectrum of the calibration lamps used to construct the flatfields themselves. However, Jupiter's spectrum is different, particularly near methane absorption bands, requiring additional correction. Our FQ889N images were corrected by about 2%, using preliminary fringing flatfields (Wong 2011) generated using the disk-averaged reflectance spectrum of Jupiter (Karkoschka 1998) convolved with the solar spectrum (Colina et al. 1996).

After corrections, each image was navigated to find the planet center using iterative ellipsoid limb fitting with Jupiter's known radii and geocentric distance and assigned proper sub-Earth and sub-solar latitude and longitude. Navigated images were then adjusted for limb darkening using a Minnaert approximation (ratio of the cosines of the incident and emission

angles raised to the  $k$  power) with the  $k$  coefficients listed in Table 1, and projected onto planetographic cylindrical maps. These maps were then mosaicked in each wavelength, except F467M, which was saturated, to produce global maps for further analysis, Figures 1(a) and (b). These maps are publicly available at <https://archive.stsci.edu/prepds/opal/>.

### 3. ANALYSES AND RESULTS

#### 3.1. Zonal Wind Field

Jupiter's zonal wind profile is known to be relatively stable with time, with only small ( $10\text{--}20\text{ m s}^{-1}$ ) variations at some wind jet peaks (Limaye 1989; Simon-Miller & Gierasch 2010; Asay-Davis et al. 2011). The OPAL data set will allow for the retrieval of a full two-dimensional wind field, requiring iterative automated retrievals to generate sufficient density of wind vectors. However, a quick comparison of the zonal wind field can be performed with a simple cross-correlation between the two global maps. Figure 2 shows such a correlation, computed from  $360^\circ$  of longitude and at every  $0.1^\circ$  of latitude, using the global maps in the F631N filter; the retrieved zonal wind is plotted at the displacement with maximum correlation (solid black line). While the profile retrieval can be further refined, the preliminary result shows very good agreement with both the *Cassini* (blue line, Porco et al. 2003) and *Voyager* (red line, Simon-Miller & Gierasch 2010) zonal wind profiles. Manual measurements (plus symbols) indicate that the changes in the zonal jets, compared with *Voyager* and *Cassini* are real.

Notably, the peak of the  $24^\circ$  N jet is at about  $153\text{ m s}^{-1}$ , between the *Cassini* and *Voyager* values of  $138$  and  $184\text{ m s}^{-1}$ , respectively. Other jets' differences are due, in part, to differences in the presence of features with distinct drift rates in the different epochs. For example, near  $7^\circ$  S, the Hubble data show a higher zonal average, but the large South Equatorial disturbance, visible during *Voyager* and again during *Cassini* was not present in 2015; it moves more slowly than the zonal wind, and may be related to large wave phenomena (Beebe et al. 1989; Simon-Miller et al. 2012). Changes in other jets require a more detailed analysis of the cloud features, retrieval of the full 2D wind circulation, and masking of vortices and other discrete features with distinct drift rates (e.g., Asay-Davis et al. 2011; Barrado-Izagirre et al. 2013), efforts that are beyond the scope of this initial report.

#### 3.2. Spectral Comparisons

As the map in Figure 1 shows, many red features are visible for spectral analysis. The Great Red Spot (GRS) still appears very orange, as it did in 2014 (Simon et al. 2014). Oval BA, to its southeast, is somewhat paler, with a whitish core and fainter orange annulus. The North Equatorial Belt (NEB) and cyclonic barges in the northern hemisphere remain the visibly reddest features on the planet (Sanchez-Lavega et al. 2013; Simon et al. 2015b). Filters in the OPAL program were specifically chosen to allow comparison of the spectral characteristics of these features with previous data sets. Figure 3 shows the 2015 OPAL data (red symbols) of the core of the GRS and reddest regions of the NEB with other data sets from 1995 to 2014. Note that the F467M filter was saturated across much of the planet, but red regions far from the saturation were usable.

The overall UV to green absorption in the GRS remains consistent with measurements from 2014, though the 889-nm methane absorption band brightness has returned to its pre-

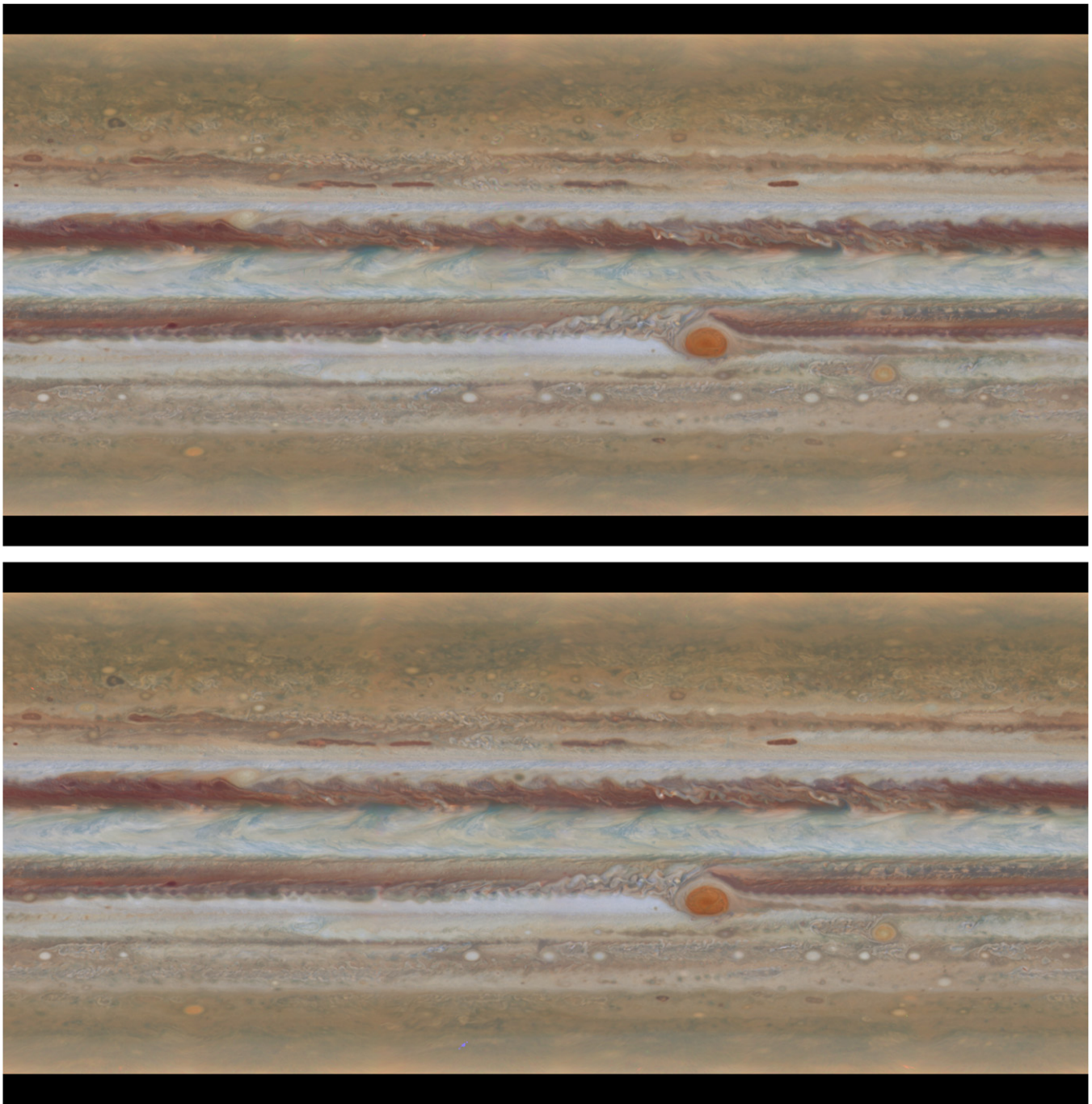


**Figure 1.** Jupiter global map from Hubble OPAL data, Rotation 1. Images are mapped between  $79^{\circ}9$  N and  $79^{\circ}9$  S latitude at  $0^{\circ}1$ /pixel resolution and color is constructed from red = 631, green = 502, and blue = 395-nm maps, respectively. (b) The same as Figure 1(a), from Rotation 2.

2014 value, indicating less haze reflectivity compared with 2014. The evolution of the GRS—a color change coincident with increased haze reflectivity, followed by a decrease in haze but constant color—is distinctly different from the evolution of other Oval BA (the smaller red storm to the south and east in Figure 1), where a one time color change occurred along with no change in haze reflectivity (Wong et al. 2011). These details may prove important in determining the identity and controlling processes of red chromophores on Jupiter, as well as the evolution of large anticyclones. The NEB spectrum remains nearly constant at all wavelengths.

### 3.3. GRS Properties

Hubble data in 2014 confirmed that the GRS’s longitudinal width has decreased significantly since 2012 (Simon et al. 2014). In 2015 it spanned  $13^{\circ}9$  of longitude and  $9^{\circ}7$  of latitude. This represents a return to the normal longitude shrinkage rate of  $\sim 0^{\circ}.19$ /year, while the latitude extent increased slightly over the 2014 measurements. It is currently centered near  $22^{\circ}4$  S latitude, and its color indicates that there is still decreased interaction with the nearby zonal wind jets (Simon et al. 2014). The time resolution of the Hubble observations are not sufficient to determine whether the

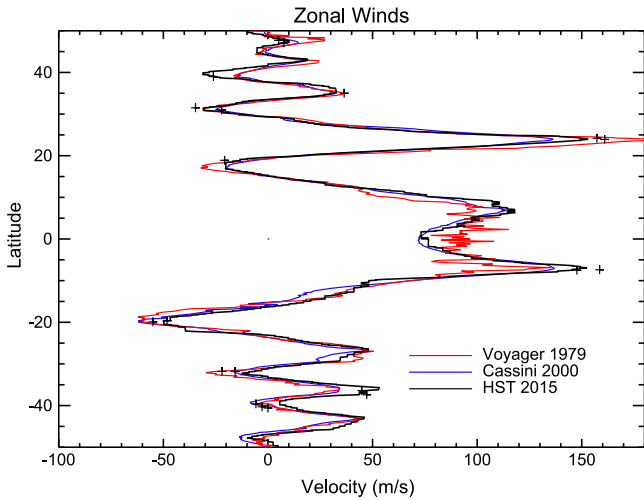


**Figure 2.** Hubble wind profile found from cross-correlation of the maps in Figure 1. The blue line is the *Cassini* profile in late 2000 (Porco et al. 2003) and the red line is from *Voyager* in 1979 (Simon-Miller & Gierasch 2010). The new wind profile matches previous profiles at most latitudes; manual measurement checks of wind jet magnitude are shown by + symbols.

observed size/shape changes have any periodic components analogous to oscillations seen by *Voyager* in Neptune’s Great Dark Spot (Smith et al. 1989; LeBeau & Dowling 1998).

An interesting feature in the 2015 data, however, is the internal GRS appearance. The core region, usually the most prominent at violet wavelengths, has been gradually shrinking, concurrent with its overall size changes (see Simon-Miller et al. 2002, Figure 3). By 2014, this separate core was largely absent (Simon et al. 2014), and, in 2015, filamentary structures can be seen spiralling near the core, Figure 4. Over 10 hours, the

motion in this structure is apparent. It was not possible to retrieve a detailed velocity field in 2014, due to Ganymede’s shadow in the region, but the velocities that were measured were consistent with previous measurements. Preliminary manual measurements confirm velocities in the range of  $100\text{--}150\text{ m s}^{-1}$ , as expected, but the OPAL data will enable later detailed flow field mapping.

### 3.4. Baroclinic Instability and Waves

The OPAL data also show a feature not previously observed in Hubble images, a small-scale wave in the NEB, see Figures 5 and 6. These fine-scale waves reside in the cyclonic region of the wind field, below several anticyclones to the north and at the same latitudes as a series of small cyclonic cells, as denoted in Figure 5. They are visible in both global maps, and at all continuum wavelengths from 343 to 658 nm; they may be visible at 275 and 889-nm, though at very low contrast levels. The features have a wavelength of about  $1^\circ$  (1200 km), larger than the 300 km mesoscale waves seen in *Voyager* and *New Horizons* data (Hunt & Muller 1979; Reuter et al. 2007; Simon et al. 2015a).

As shown in Figure 6, these waves span  $\sim 2^\circ\text{--}3^\circ$  of latitude covering the cyclonic flank of the westward jet that peaks at  $17^\circ$  N. Although the wave is visible in multiple images, it is difficult to identify the same wave crests from frame to frame in large time separations, even in the filter with best contrast, F395N, Figure 6 middle and bottom panels. Wave crest identification is not unique over a 20-hr separation and no detectable wave motions were possible. Short 1-hr time separations are too short to confirm velocities, given the large velocity uncertainties over such a short time period at the available spatial resolution.

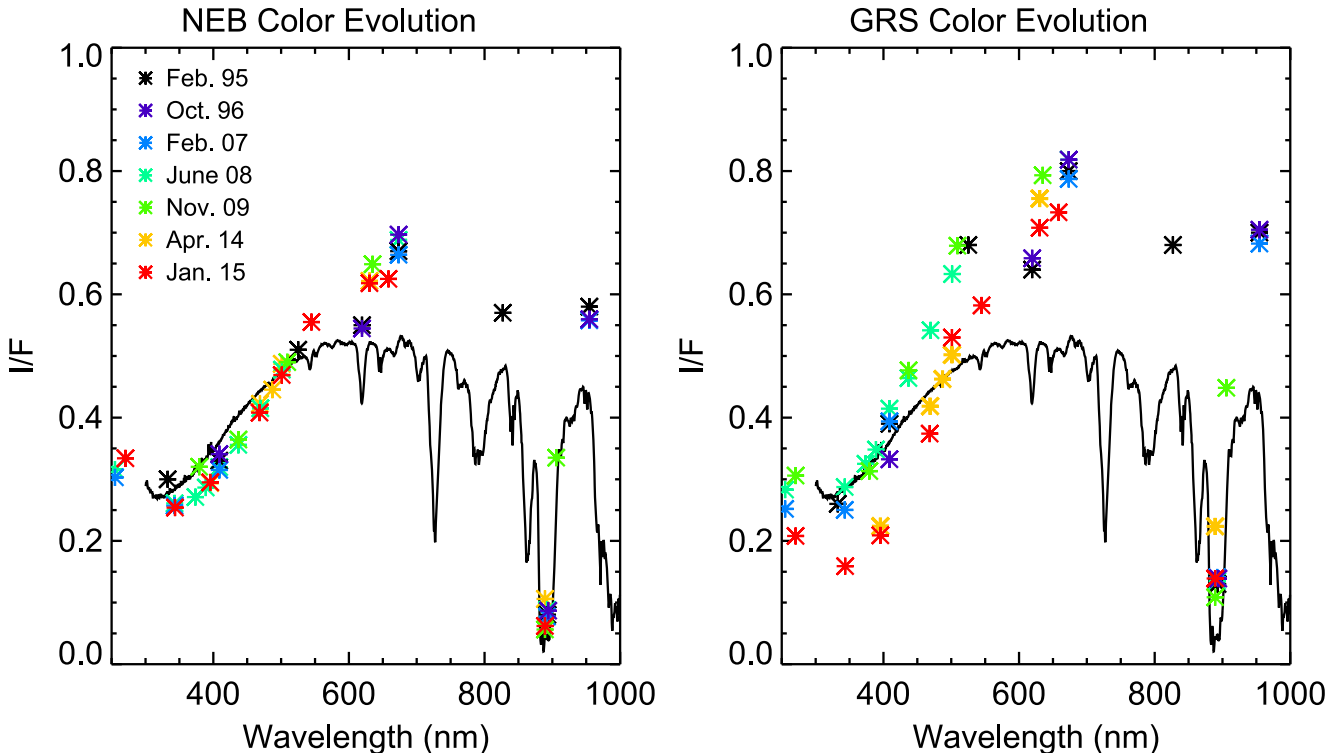


**Figure 3.** Reflectance spectra of the North Equatorial Belt and Great Red Spot from 1995 to 2015. The darkest spots of the NEB remain stable in color, while the GRS retains the increased blue absorption seen in 2014.

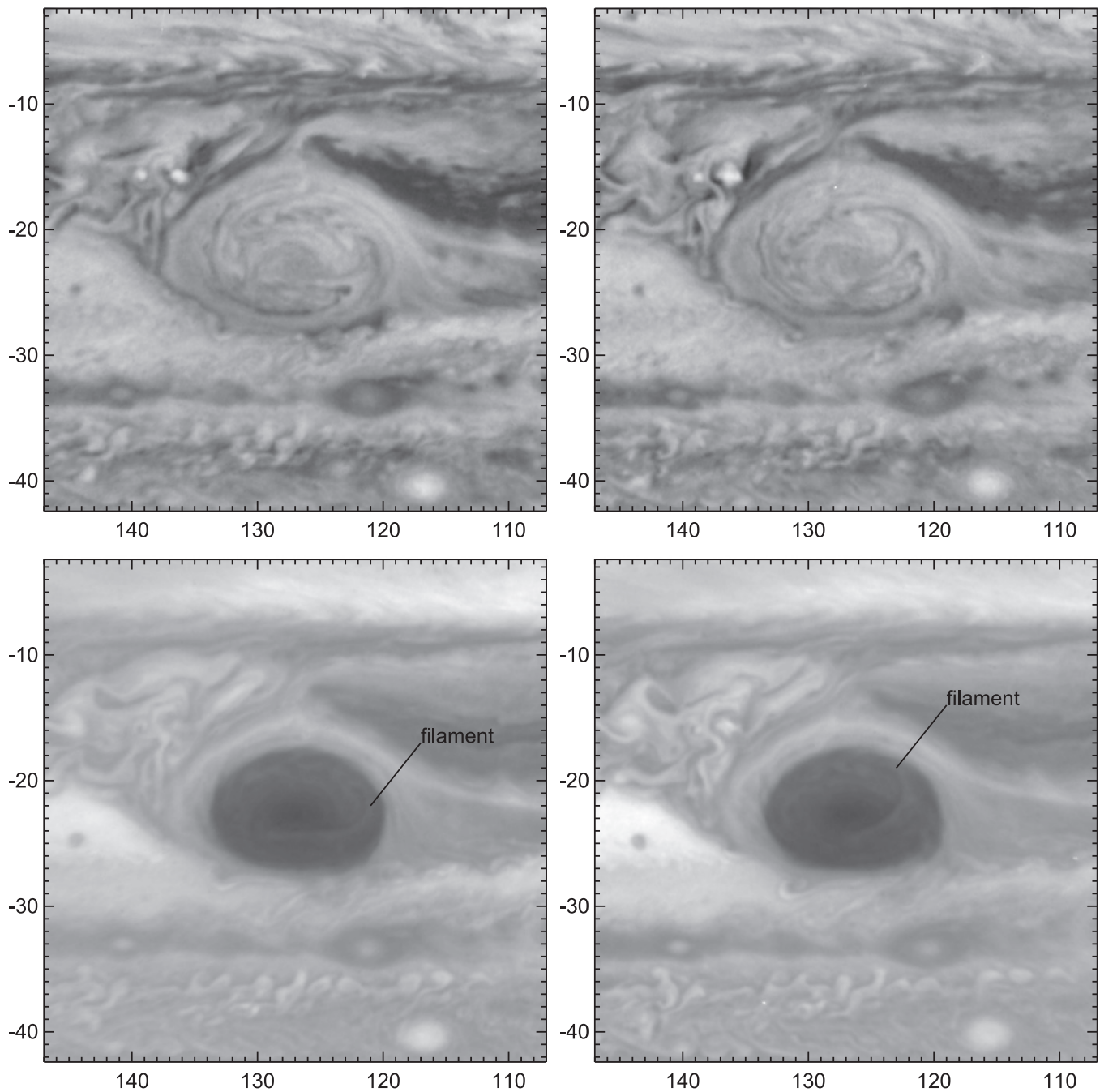


**Figure 4.** Jupiter’s Great Red Spot in F395N (bottom) and F631N (top), with System III W. longitude and planetographic latitude labeled. The left panels are from the first rotation, and the right panels are 10 hr later. Internal structures in the right panels have rotated counterclockwise relative to the left panels.

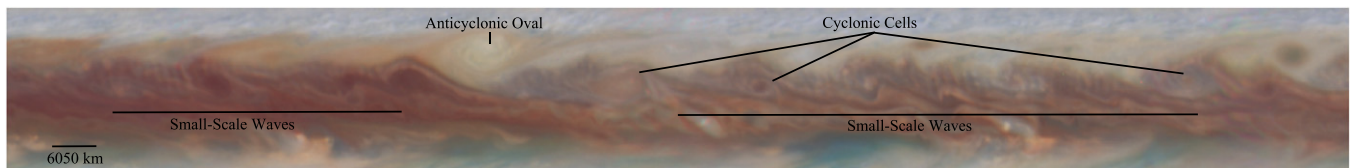


**Figure 5.** Limited longitude region centered on 16° N latitude. Small-scale waves are superimposed on other cloud structures in the North Equatorial Belt, including cyclones at the same latitude. Anticyclones are visible to the north corresponding to the anticyclonic shear region of the background wind field.

This type of wave is similar in appearance to terrestrial wave formation in a baroclinic instability (see Holton 1992, Figure 6.5). On the Earth, baroclinic instabilities explain mid- to high-latitude cyclone generation, and waves form along with cyclonic features

(Charney 1947; Eady 1949). On the giant planets, such instabilities may play a role in wind jet formation (e.g., Kaspi & Flierl 2007). Using the Earth analogy, we can examine the characteristics of the OPAL wave for consistency with a baroclinic wave.

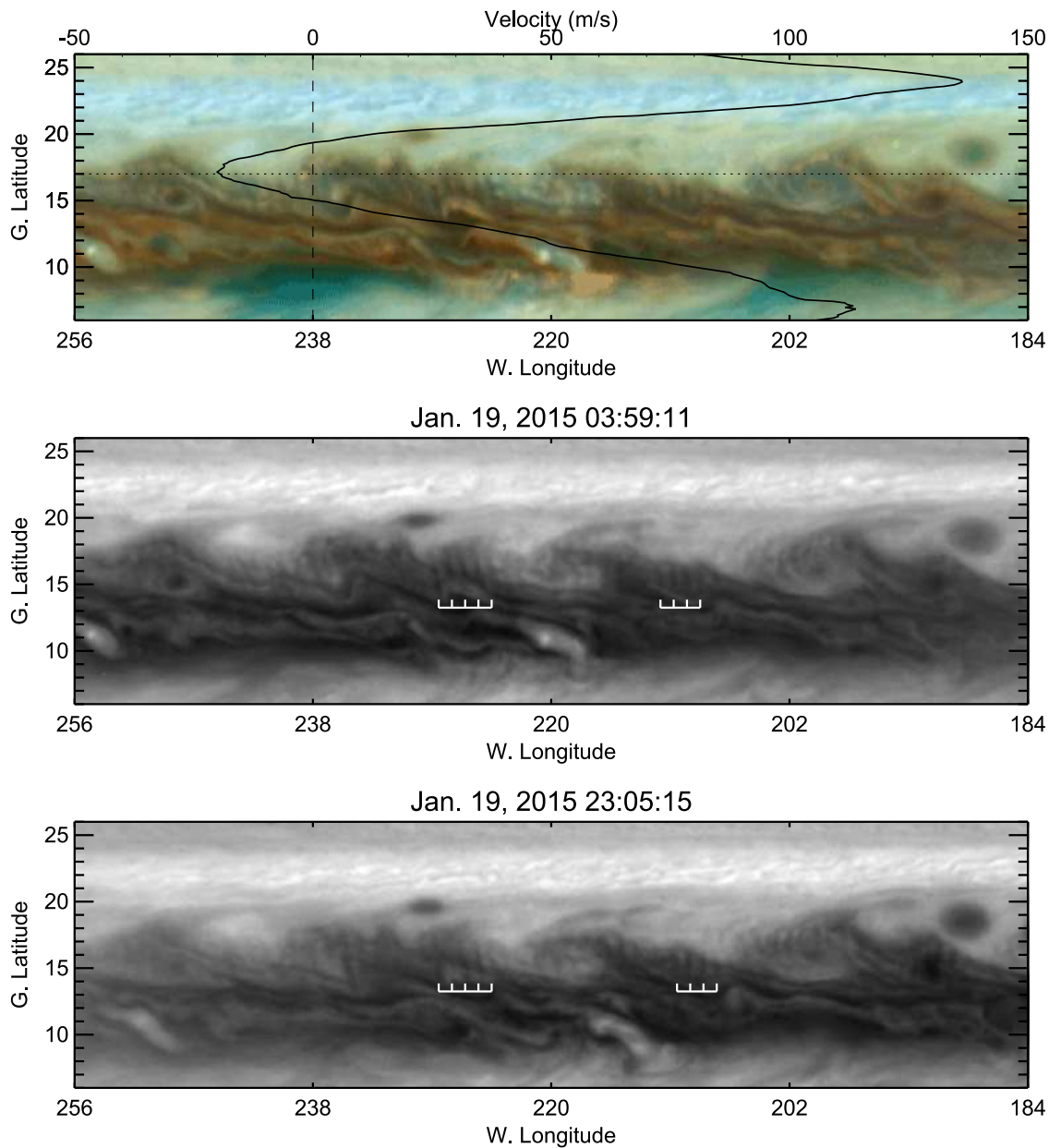


**Figure 6.** Wave crest location and evolution. In the top panel, the *Cassini* wind profile is plotted over a color map, showing that the waves reside in the cyclonic shear region. The middle and bottom panels show F395N maps 20 hr apart, showing that little wave evolution or motion has occurred.

One diagnostic is the meridional size of the wave features. Stone (1969) showed that for most baroclinic waves, the meridional scale should be on the order of the radius of deformation. However, Simmons (1974) showed that if the jet width scale is larger than the deformation radius, the wave’s meridional extent can be between the two in scale.

Gierasch et al. (1979) modeled Jupiter’s atmosphere using a nearly adiabatic deep layer beneath the clouds. Unlike the Eady (1949) terrestrial model with a rigid lower boundary, this scheme had drastically reduced growth rates of baroclinic instabilities due to the influence of the deep neutrally stable layer. Conrath et al. (1981) examined this again and found that for westward jets that are broad (where the deformation scale is much smaller than the jet width), the Eady modes are still suppressed, but Charney modes (Charney 1947) are allowed and the disturbance can be a mix of barotropic and baroclinic instabilities if deformation radius and jet width are comparable.

The main difference between the Eady and Charney modes is the influence of the gradient of the Coriolis parameter, which makes Charney mode growth less dependent on the bottom boundary condition. Conrath et al. (1981) hypothesized that the jet widths in Jupiter’s atmosphere, at least 3–10 times the tropospheric deformation radius, would enable transfer of energy from eddies to jets. Instabilities are baroclinic within this range.

The atmospheric radius of deformation is defined as

$$L = NH/|f|,$$

where  $N$  is the Brunt–Vaisala frequency,  $H$  is the scale height, and  $f$  is the Coriolis parameter. The Coriolis parameter,  $f$ , is  $9.1 \times 10^{-5} \text{ s}^{-1}$  at  $15^\circ \text{ N}$  planetographic latitude. The pressure scale height,  $H = k_B T/mg$ , is 25 km, using a temperature of 160 K (near the  $\text{NH}_3$  cloud base), an effective gravity of

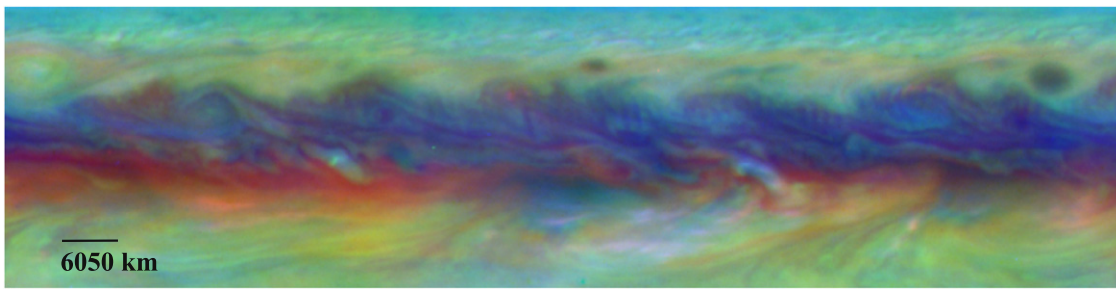


**Figure 7.** False color map of the wave region with red = 889 nm, green = 502 nm, and blue = 275-nm images. Wave shifts in altitude would be apparent as color changes along or across a wave crest; none are apparent. The highest thick clouds are white/yellow deep clouds covered with haze/aerosol are blue, and red areas indicate regions of high cloud but less haze.



**Figure 8.** *Voyager 2* image centered near 16° N latitude. This image was acquired on 1979 July 3 in the violet filter and shows a faint wave train of a similar scale as one as seen in the Hubble data. Note that this image is not shown at the same scale as the Hubble data.

$22.88 \text{ m s}^{-2}$  for 15° latitude, and a mean molecular mass of 2.30 Da assuming *Galileo* Probe composition (Niemann et al. 1998; Mahaffy et al. 2000; Wong et al. 2004). The Brunt–Vaisala frequency,  $N$ , describes the static stability of the atmosphere, and has been constrained by a number of methods in Jupiter’s atmosphere, including models of cloud formation and vortex circulation, and temperature profiles measured by radio occultations, infrared spectroscopy, and in situ measurement by the *Galileo* Probe; typical values of  $N$  range from 2 to  $12 \times 10^{-3} \text{ s}^{-1}$  in and between the cloud layers, to 1.6 and to  $2.3 \times 10^{-2} \text{ s}^{-1}$  at 250 mbar just below the tropopause (Wong 2011; Watkins & Cho 2013 and references therein). The atmospheric deformation radius near the  $\text{NH}_3$  cloud base is then around 1400 km if cloud condensation creates stability, or 500 km in the free air below this cloud level. The wind jet spans 4.5 of latitude or  $\sim 5000$  km, just broad enough to meet the minimum 3–10  $L$  criterion for possible energy transport from eddies to jets (Conrath et al. 1981). The waves span 2000–3000 km, and are thus consistent with the Simmons (1974) model of the meridional scale of baroclinic instabilities.

Additionally, on Earth, baroclinic instabilities tilt westward and northward with altitude (e.g., Lim & Wallace 1991; Yin & Battisti 2004). The Hubble images at 889 and 275 nm are more sensitive to higher altitudes, but both have little high contrast detail and also show underlying cloud structure, so any such tilts are not obvious, see Figure 7. However, some of the wave crests do have a slight westward tilt with the zonal wind pattern, Figure 5, while others near the cyclone at 202° W are curved. This is consistent with theoretical

models (Holton 1992) and Earth observations (e.g., Blackmon et al. 1984).

#### 4. DISCUSSION

One aspect that is unclear is the exact atmospheric conditions needed for baroclinic wave formation on Jupiter. Waves of this type have not been seen on other dates in Hubble imaging from 1994 to 2014 nor by the *Galileo* or *Cassini* spacecraft. The one exception is during *Voyager 2*, where a similar, but very faint, feature was briefly observed with 700–1000-km wavelength at these latitudes (Smith et al. 1979, Figure 8). It was seen 10 hr later, and possibly after several days, but only over a limited longitudinal region. However, during the *Voyager 1* flyby several months earlier, and Hubble observations in 1994–1996, the region had similar anticyclone/cyclone patterns and zonal wind magnitudes, and yet the wave structure was not observed. Other concurrent atmospheric conditions, such as temperature variations, must be necessary for wave formation/visibility.

Baroclinic instabilities with  $\sim 1200$  km wavelength have growth times of about 30 days and correspond to a Brunt–Vaisälä frequency of  $N = 0.0014 \text{ s}^{-1}$  in the level where the instability is seated, in the model of Conrath et al. (1981). Conditions are therefore typical of the free air between major cloud layers because  $N$  within cloud layers is significantly greater, on the order of  $0.005\text{--}0.01 \text{ s}^{-1}$  (Wong 2011). This presents an interesting problem: static stability must be weak, calling for an altitude that is well separated vertically from the cloud condensation layers. However, the wave must be propagating at an altitude where clouds do condense, or else there would be no visible wave tracers. This seeming

contradiction may play a role in the apparent rarity of this type of wave structure. We may be observing a disturbance that is seated in a weakly stratified layer between cloud decks, but can only be observed when it propagates vertically into a cloud condensation level. Achterberg & Ingersoll (1989) emphasized the sensitivity of baroclinic instabilities to stratification and wind shear, suggesting that future numerical simulations may further test the vertical profiles of temperature and horizontal velocity needed to generate these features.

## 5. SUMMARY

The OPAL program has begun its yearly campaign of high-resolution imaging of the outer planets. Jupiter data acquired in 2015 are already yielding new results, as well as adding to the long-term monitoring of the atmospheric state. Within navigation uncertainties, our initial analysis finds a zonal wind profile identical to the *Voyager* and *Cassini* era profiles at most latitudes, with some variation in mid- to high-latitude wind jet magnitudes, particularly at  $+40^\circ$  and  $-35^\circ$  planetographic latitude. Further analyses will focus on the complete two-dimensional wind field.

In addition, the GRS has maintained the intense orange coloration first observed in 2014, and interpreted as decreased interaction with nearby wind jets. It also shows new internal structures and an almost lack of its usual distinct core. The internal velocity field will need to be examined to determine if there has been any significant change from previous measurements.

Finally, a wave feature was also observed near  $16^\circ$  N latitude, similar to a faint feature observed in *Voyager 2* images. It is likely caused by a baroclinic instability that also forms cyclones, as on Earth and in agreement with Jupiter analytical models. Further numerical simulation will be needed to explain why such a feature is not often observed, despite outwardly similar environmental conditions on other dates.

This work was based on observations made with the NASA/ESA *Hubble Space Telescope* under program GO13937. Support for this program was provided by NASA through a grant from the Space Telescope Science Institute, which is operated by the Association of Universities for Research in Astronomy, Inc., under NASA contract NAS5-26555. A.A.S. thanks Peter Gierasch for informative discussions about wave formation and baroclinic instabilities.

## REFERENCES

- Achterberg, R. K., & Ingersoll, A. P. 1989, *JAtS*, **46**, 2448  
 Asay-Davis, X. S., Marcus, P., Wong, M. H., & de Pater, I. 2011, *Icar*, **211**, 1215  
 Barrado-Izagirre, N., Rojas, J. F., Hueso, R., et al. 2013, *A&A*, **554**, A74  
 Beebe, R. F., Orton, G. S., & West, R. A. 1989, Time Variable Phenomenon in the Jovian System, **245**  
 Blackmon, M. L., Lee, Y.-H., & Wallace, J. M. 1984, *JAtS*, **41**, 961  
 Charney, J. G. 1947, *J. Meteorology*, **4**, 135  
 Colina, L., Bohlin, R. C., & Castelli, F. 1996, *AJ*, **112**, 307  
 Conrath, B. J., Gierasch, P. J., & Nath, N. 1981, *Icar*, **48**, 256  
 Dressel, L. 2015, Wide Field Camera 3 Instrument Handbook, Version 7.0 (Baltimore: STScI) [http://www.stsci.edu/hst/wfc3/documents/handbooks/currentIHB/wfc3\\_cover.html](http://www.stsci.edu/hst/wfc3/documents/handbooks/currentIHB/wfc3_cover.html)  
 Eady, E. T. 1949, *Tell*, **1**, 38  
 Gierasch, P. J., Ingersoll, A. P., & Pollard, D. 1979, *Icar*, **40**, 205  
 Holton, J. R. 1992, An Introduction to Dynamic Meteorology (3rd ed.; New York: Academic)  
 Hunt, G. E., & Muller, J.-P. 1979, *Natur*, **280**, 778  
 Karkoschka, E. 1998, *Icar*, **133**, 134  
 Kaspi, Y., & Flierl, G. R. 2007, *JAtS*, **64**, 3177  
 LeBeau, R. P., & Dowling, T. E. 1998, *Icar*, **132**, 239  
 Lim, G. H., & Wallace, J. M. 1991, *JAtS*, **48**, 1718  
 Limaye, S. S. 1989, Time Variable Phenomenon in the Jovian System, **311**  
 Mahaffy, P. R., Niemann, H. B., Alpert, A., et al. 2000, *JGRE*, **105**, 15061  
 Niemann, H. B., Atreya, S. K., Carignan, G. R., et al. 1998, *JGR*, **103**, 22831  
 Porco, C. C., West, R. A., McEwen, A., et al. 2003, *Sci*, **299**, 1541  
 Reuter, D. C., Simon-Miller, A. A., & Lunsford, A. 2007, *Sci*, **318**, 223  
 Sanchez-Lavega, A., Legarreta, J., Garcia-Melendo, E., et al. 2013, *JGRE*, **118**, 1  
 Simmons, A. J. 1974, *JAtS*, **31**, 1515  
 Simon, A. A., Li, L., & Reuter, D. C. 2015a, *GeoRL*, **42**, 2612  
 Simon, A. A., Sanchez-Lavega, A., Legarreta, J., et al. 2015b, *JGRE*, **120**, 483  
 Simon, A. A., Wong, M. H., Rogers, J. H., et al. 2014, *ApJL*, **797**, L31  
 Simon-Miller, A. A., & Gierasch, P. J. 2010, *Icar*, **210**, 258  
 Simon-Miller, A. A., Gierasch, P. J., Beebe, R. F., et al. 2002, *Icar*, **158**, 249  
 Simon-Miller, A. A., Rogers, J. H., Gierasch, P. J., et al. 2012, *Icar*, **218**, 817  
 Smith, B. A., Soderblom, L. A., Banfield, D., et al. 1989, *Sci*, **246**, 1422  
 Smith, B. A., Soderblom, L. A., Beebe, R. F., et al. 1979, *Sci*, **206**, 927  
 Stone, P. H. 1969, *JAtS*, **26**, 376  
 Watkins, C., & Cho, J. Y.-K. 2013, *GeoRL*, **20**, 472  
 Wong, M. H. 2010, Amplitude of Fringing in WFC3/UVIS Narrowband Red Filters, Instrument Science Rep. WFC3 2010-04 (Baltimore, MD: Space Telescope Science Institute)  
 Wong, M. H. 2011, in Proc. 2010 STScI Calibration Workshop, Fringing in the WFC3/UVIS Detector, ed. S. Deustua & C. Oliveira (Baltimore, MD: Space Telescope Science Institute)  
 Wong, M. H., de Pater, I., Asay-Davis, X. S., Marcus, P. S., & Go, C. Y. 2011, *Icar*, **215**, 211  
 Wong, M. H., Mahaffy, P. R., Atreya, S. K., Niemann, H. B., & Owen, T. C. 2004, *Icar*, **171**, 153  
 Wong, M. H., Simon, A. A., Orton, G. S., de Pater, I., & Sayanagi, K. M. 2015, in 46th Lunar and Planetary Science Conf., LPI Contribution No. 1777, 2606 <http://www.lpi.usra.edu/publications/abstracts.shtml>  
 Yin, J. H., & Battisti, D. S. 2004, *JAtS*, **61**, 1454